

Variability of stellar granulation and convective blueshift with spectral type and magnetic activity.[★] I. K and G main sequence stars

N. Meunier¹, A.-M. Lagrange¹, L. Mbemba Kabuiku¹, M. Alex¹, L. Mignon¹, S. Borgniet¹

Univ. Grenoble Alpes, CNRS, IPAG, F-38000 Grenoble, France
e-mail: nadege.meunier@univ-grenoble-alpes.fr

Received 3 June 2016 ; Accepted 21 September 2016

ABSTRACT

Context. In solar-type stars, the attenuation of convective blueshift by stellar magnetic activity dominates the *RV* (radial velocity) variations over the low amplitude signal induced by low mass planets. Models of stars that differ from the Sun will require a good knowledge of the attenuation of the convective blueshift to estimate its impact on the variations.

Aims. It is therefore crucial to precisely determine not only the amplitude of the convective blueshift for different types of stars, but also the dependence of this convective blueshift on magnetic activity, as these are key factors in our model producing the *RV*.

Methods. We studied a sample of main sequence stars with spectral types from G0 to K2 and focused on their temporally averaged properties: the activity level and a criterion allowing to characterise the amplitude of the convective blueshift. This criterion is derived from the dependence of the convective blueshift with the intensity at the bottom of a large set of selected spectral lines.

Results. We find the differential velocity shifts of spectral lines due to convection to depend on the spectral type, the wavelength (this dependence is correlated with the *T_{eff}* and activity level), and on the activity level. This allows us to quantify the dependence of granulation properties on magnetic activity for stars other than the Sun. We are indeed able to derive a significant dependence of the convective blueshift on activity level for all types of stars. The attenuation factor of the convective blueshift appears to be constant over the considered range of spectral types. We derive a convective blueshift which decreases towards lower temperatures, with a trend in close agreement with models for *T_{eff}* lower than 5800 K, but with a significantly larger global amplitude. Differences also remain to be examined in detail for larger *T_{eff}*. We finally compare the observed *RV* variation amplitudes with those that could be derived from our convective blueshift using a simple law and find a general agreement on the amplitude. We also show that inclination (viewing angle relative to the stellar equator) plays a major role in the dispersion in *RV* amplitudes.

Conclusions. Our results are consistent with previous results and provide, for the first time, an estimation of the convective blueshift as a function of *T_{eff}*, magnetic activity, and wavelength, over a large sample of G and K main sequence stars.

Key words. Physical data and processes: convection – Techniques: radial velocities – Stars: magnetic field – Stars: activity – Stars: solar-type – Sun: granulation

1. Introduction

The understanding of stellar activity and its impact on convection is an important challenge when studying the impact of stellar activity on exoplanet detectability because the variability of the convection attenuation impacts stellar radial velocities (*RV*s). In the solar case, the inhibition of convection by magnetic fields indeed dominates the stellar signal (Meunier 2010a). This model has been confirmed with several observations: the reconstruction of the solar *RV* using Michelson Doppler Imager (MDI) Dopplergrams (Meunier 2010; more recently, *RV* variations of similar amplitude have been obtained using direct observations of the Sun (Jordum et al. 2015) as well as using indirect solar *RV* measurements from various bodies in solar system observations (Moon, asteroids, Jupiter satellites) by (Meunier et al. 2015) and (Meunier et al. 2016).

In simulations made by (Meunier et al. 2015) based on observed solar features and later by (Meunier et al. 2016) based on simulated solar features, it was assumed that the solar convective blueshift was attenuated by a factor of

two thirds, on average, in magnetic regions such as plages and the solar network, based on solar observations by (Meunier et al. 2015). How stellar granulation changes with magnetic field for different stellar types is yet unknown. This is, however, a critical factor in estimating the impact of stellar type on the activity-induced *RV* variations, as already pointed out by (Meunier et al. 2015), for example by extrapolating the work of (Meunier et al. 2015) to stars other than the Sun.

The determination of the amplitude of the absolute convective blueshift depends on two parameters, for a given coverage by magnetic features: 1/ How does the convective blueshift depend on spectral type? 2/ Is the attenuation factor, due to magnetic fields, similar for all stars?

Concerning the first issue, a number of results in the literature already give some clues. (Meunier et al. 2015) have shown that the dependency of the velocity derived from each spectral line as a function of their depth is directly related to the properties of solar convection. Lines of different depths (intensities) form at different depths in the atmosphere: they are therefore probing regions with different intensity-velocity correlations inside granules, so that their sensitivity differs for different convective blueshifts. Two types of measurements reflect this process: 1/ the absolute shifts of spectral line bisectors; 2/ the differential velocity shifts

Send offprint requests to: N. Meunier

[★] Tables A.1 and B.1 are only available in electronic form at the CDS via anonymous ftp to cdsarc.u-strasbg.fr (130.79.128.5) or via <http://cdsarc.u-strasbg.fr/viz-bin/qcat?J/A+A/>

of spectral lines (namely between lines of different depths). The first ones are difficult to measure because of other effects not easy to quantify at the required precision (except for the Sun). The latter seems to have a universal shape according to ? ? also show that the bottom of the line position is less sensitive to resolution effects compared to the bisector analysis, which is also interesting when studying a large sample of stars with different $v \sin i$, making it a powerful method to estimate these convection properties, something not possible by RV jitter analysis.

This property has been studied for stars other than the Sun ?, e.g. [gray82, dravins87b, dravins99, hamilton99, landstreet07, allendeprieto02, gray09] but always for a very small number of main sequence stars. The analysis has usually been performed using a very small number of lines, ?, or low signal to noise ratio (S/N) spectra. How the measurements are impacted by the choices of selected lines has not been investigated so far. These studies however show that velocity flows inside granules and resulting convective blueshifts increase with T_{eff} . ? have studied a larger sample but found a very large dispersion of the convective blueshift of the main sequence stars. On the other hand, recent hydrodynamical numerical simulations have been performed by ? and show a clear dependence of the convective blueshift on spectral type. Other groups have performed hydrodynamical simulations of granulation over a grid of stellar parameters; ?, ?, ?, ?, ?, but do not provide potentially useful values of the convective blueshift. ? however found larger granules (usually associated with larger velocity fields) for hotter stars, consistent with a larger convective blueshift. In principle both effects (absolute and differential velocity shifts) can be extracted from numerical simulations providing they model enough spectral lines: this is discussed in Sect. 4.

Concerning the second issue however, it is mostly uncharted and no previous study has estimated whether the response of the granulation to magnetic field depends on the spectral type or not. Several studies have aimed at measuring the temperature variations of individual stars during stellar cycles ?, [gray92, gray94, gray95, gray96a, gray96], yet no systematic tendency is available today.

In this paper we therefore focus on this last aspect. We aimed to precisely estimate the convective blueshift for a large sample of G-K main sequence stars but also measure how this blueshift varies with magnetic activity. To this end, we measured the differential velocity shifts of spectral lines, and more specifically their slope, defined in a robust way, in order to estimate the amplitude of granulation for each star. After a description of our data analysis in Sect. 2, we derive the dependency on spectral type and activity level of the granulation amplitude using this criterion in Sect. 3. We focus on the temporally-averaged properties of stars: average activity level and convective level. Then in Sect. 4, we propose an estimation of the absolute shifts of spectral line bisectors from the criterion estimated in Sect. 3, using the Sun as a reference and adopting some assumptions. Finally, in Sect. 5 we reconstruct RV amplitudes as a function of the activity variability amplitude. The RV jitters as a function of *average* activity level have been studied in the past, but seldomly as a function of the amplitude activity amplitude. We conclude in Sect. 6.

2. Data analysis

2.1. Data sample

We have extracted 167 stars, grouped into six samples from the HARPS survey described in ?, and covering the spectral types

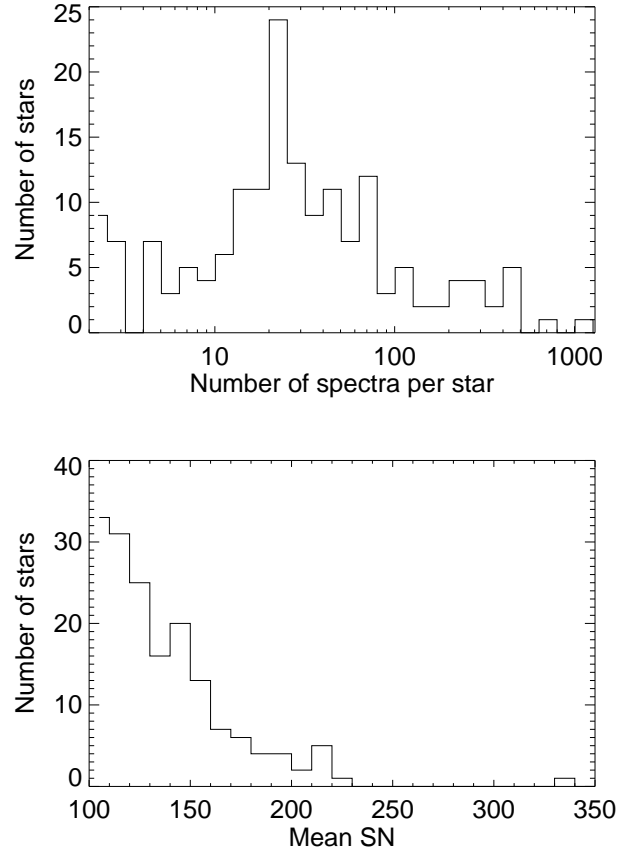


Fig. 1. *Upper panel:* Distribution of the number of spectra per star. *Lower panel:* Distribution of the average S/N per star.

Table 1. Sample characteristics

Sp. T.	N_{Star}	N_{Spectra}	N_{Lines}	$\langle T_{\text{eff}} \rangle$	$\langle B-V \rangle$
G0 V	41	2664	152	5872	0.606
G2 V	31	2386	148	5815	0.626
G5 V	31	953	153	5665	0.678
G8 V	27	2289	154	5456	0.734
K0 V	16	660	148	5327	0.797
K2 V	21	2136	169	5061	0.894
Total	167	11088	196	-	-

Notes. Temperatures are from Sousa et al (2008). B-V are from the Simbad database at the CDS.

G0, G2, G5, G8, K0, and K2. The spectral types have been extracted from the Simbad database at the CDS¹. This survey was biased against very active and young stars, and focuses on stars with $v \sin i$ lower than 3-4 km/s, as pointed out by ? in the study of cycles in stars from the same survey.

The spectra have been retrieved from the ESO archive²: We analyse 1D spectra produced by the ESO Data Reduction Software after the interpolation of the 2D echelle spectra (one spectrum per order) over a grid with a constant step in wavelength (0.01 Å). The original 2D spectra are also retrieved for the computation of the uncertainties.

¹ <http://simbad.u-strasbg.fr/simbad/>

² http://archive.eso.org/wdb/wdb/adp/phase3_spectral/form

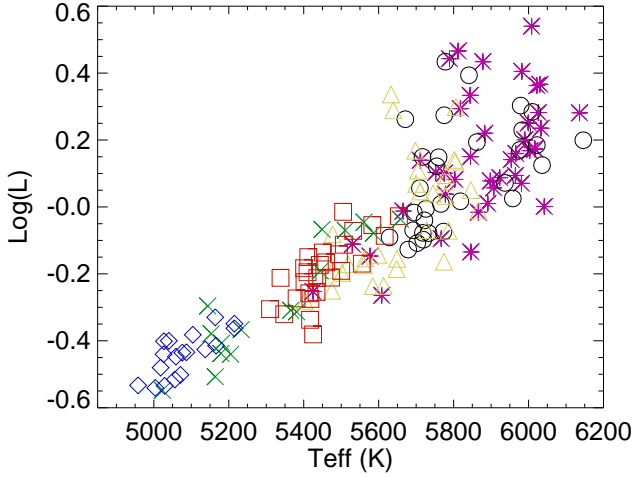


Fig. 2. Log of the luminosity (relatively to the solar luminosity) versus temperature (from Sousa et al 2008) for the main sequence stars in our six samples: G0 (pink stars), G2 (black circles), G5 (yellow triangles), G8 (red squares), K0 (green crosses), and K2 (blue diamonds).

We only retained spectra with a S/N, averaged over all orders, larger than 100. Stars with less than three such spectra were eliminated. Indeed ? insists on the need to consider only high S/N spectra for this type of analysis, especially if a small number of lines is considered. Although the S/N does not seem to bias our results, low S/N values lead to a large dispersion, which increases the uncertainties and decreases the number of spectral lines which can be analysed, hence the necessity for our threshold. Fig. 1 shows the distribution of the number of spectra per star and the average S/N per star. For most stars, we analysed between 10 and 100 spectra, the number ranging between 3 and more than 1000. The S/N values typically lie between 100 and 200.

Fig. 2 shows the luminosity versus T_{eff} for our six samples, provided by ?. The global properties of each of these samples are shown in Table 1. The B-V values have been retrieved from the CDS. The individual values for each star are indicated in Table 1.

2.2. Spectra correction and line identification

2.2.1. Continuum correction

We first normalised the spectra for the continuum in two steps: we first identified an upper envelope for each spectrum and then applied a correction factor, to take into account the fact that due to the presence of noise the actual continuum is slightly lower than this upper envelope. The procedure is described in Appendix B. We estimated that the resulting uncertainties on the intensities were usually lower than 1%, and much better at high S/N.

2.2.2. Line identification

We used a list of spectral lines of Ca, TiI, TiII, and FeII lines ?, Jdravins08, and FeI lines ?, Jnave94. Only some of these were selected for the final analysis (see 2.3). The lines were identified on each spectrum as local minima (over 41 pixels) below a flux equal to 90% of the continuum. Note that for the purpose of line identification, we shift the spectra towards a zero shift position

(with a one pixel of 0.01 Å precision) to ensure that the position of the minimum is as close as possible to the theoretical wavelength: in practice, this is done manually for one spectrum per spectral type which serves as a reference and all other spectra are shifted to match this reference spectrum. No interpolation is done, as the pixel precision is sufficient for the line identification and it does not affect the following analysis.

Before any computation on the spectral lines, we eliminated blended lines whose wavelengths were very close to each other in our list and by doing a visual inspection. Another selection using automatic criteria was then implemented (see next section).

2.3. Differential velocity shifts of spectral lines

To compute the differential velocity shifts of spectral lines, we performed a polynomial fit of the bottom of the line over five pixels (covering a range of 0.04 Å, i.e. corresponding to about 40% of the typical line width at half maximum). We then estimated the position of the minimum of the fit and by comparison with the laboratory wavelength, computed the velocity of the line. For each line we therefore derived a wavelength and its uncertainty, which we then transformed into a radial velocity RV (relative to the laboratory wavelength) and its uncertainty σ_{RV} . A similar method was also applied by ? and ?. We also derived the flux at the bottom of the line, F , and its uncertainty σ_F . We finally computed the bisector of each line, which was then used for the line selection. We note that in the red part of the optical spectrum, the presence of telluric lines may have impacted a priori our results: this is discussed in Sect. 2.5.

We then selected the lines to be used for our analysis using several automatic criteria on each line. We chose to eliminate: lines with a bisector slope outside the $3\text{-}\sigma$ range of all bisectors ?, this criteria is close to the one used bybut our threshold was not fixedJramirez08 or a rms of the bisector fit residual outside the $3\text{-}\sigma$ range; lines with a line width outside the $3\text{-}\sigma$ range where σ is deduced from the gaussian fit of the distribution of the variable.

In most of our computations (especially the slope of RV vs F) we considered only strong enough lines, that is, points with F lower than 0.6 only, except when indicated otherwise. For selection purposes, we also add a criteria based on the $RV - F$ relationship. For several lines, the RV strongly deviates from the average RV found using the other lines, meaning that such lines could also be blended. We therefore eliminated the lines with measurements outside $5\text{-}\sigma$ (around the linear fit RV versus F). Finally, lines appearing in only one star of the stellar type sample were also eliminated. This allows us to apply a robust criterion on the differential velocity shifts of spectral lines, as described in the following section. The final list of selected lines can be found in Table. 1.

2.4. A criterion to characterise the differential velocity shifts of spectral lines

An example of the differential velocity shifts of spectral lines obtained after the line selection described above is shown in Fig. 3 (upper panel) for the G2 star HD223171. Typical formal uncertainties on RV values after temporally averaging the RV obtained using the same line are in the range 5-15 m/s, while the rms around the linear fit in that example is 84 m/s. 138 lines are used in this example. The average RV computed at each time step over all selected lines has been subtracted (the zero is therefore arbitrary here). A correction using the stellar RV provided by the

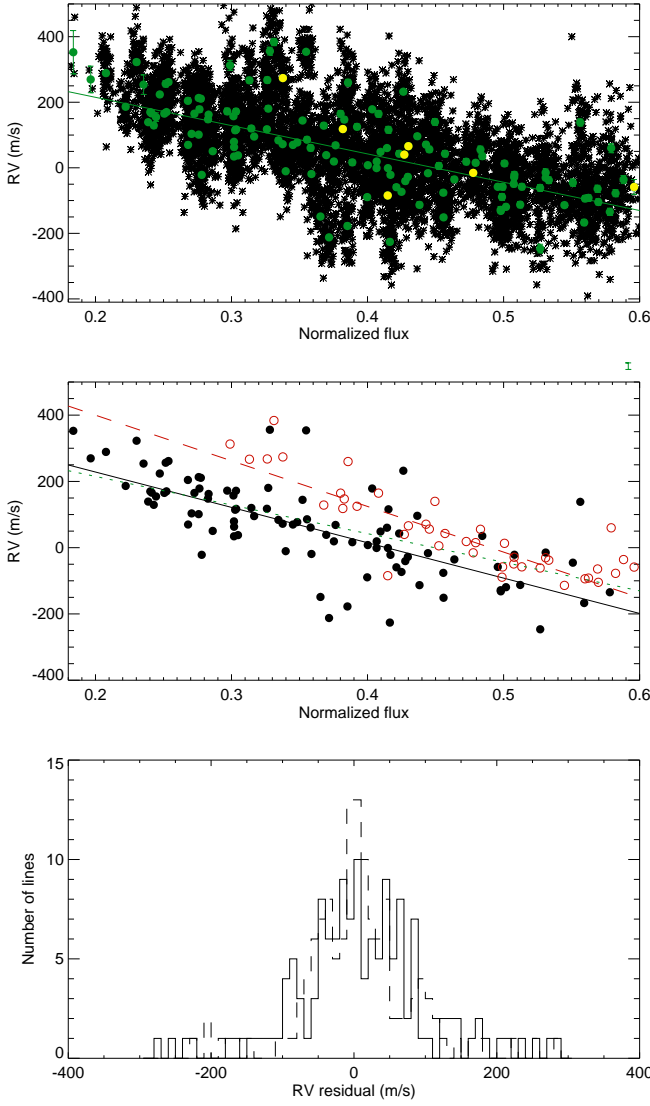


Fig. 3. *Upper panel:* RV versus a normalised flux of the bottom of the lines for HD223171 (G2), for lines deeper than the 0.6 threshold. Crosses represent individual measurements while green dots correspond to the temporal average for each line. The yellow dots are lines used by Gray (2009). The straight line is a linear fit on the green dots. *Middle panel:* Same as above but showing the wavelength dependence: The black filled circles and solid line are for lines with wavelength below 5750 Å, while the red open circles and dashed lines are for wavelengths above 5750 Å. The green dotted line is the linear fit on all points. *Lower panel:* Distribution of the RV residual after removal of the linear fit, that is, the green dots of the upper panel (solid line). The rms RV is 84 m/s. The dashed line shows the same distribution but for the residual computed after the wavelength-dependence correction (see text), and the rms RV is 78 m/s.

ESO Data Reduction Software does not change our subsequent results significantly.

The dispersion of the residual RV is important. It can be due to several factors, for example: telluric lines, impact of a wavelength dependence, uncertainties on laboratory wavelength (all discussed in Sect. 2.5), impact of blends not taken into account

or other properties of the lines, such as the excitation potential χ , Jdravins81.

We defined a criterion to easily study the shape of the differential velocity shifts of spectral lines as a function of various parameters: we computed the slope of RV versus F values after averaging all points corresponding to a given line (i.e. typically on the green points on Fig. 3). We note that the formal uncertainties for RV seem to be slightly under-estimated, as estimated by the comparison of the dispersion in RV and F for a given line and the formal uncertainties, by about a factor 1.3 on average but sometime by up to a factor 2: We therefore use the uncertainties derived from the dispersion (of the RV obtained for a given line) to avoid underestimating our uncertainties. This slope is named hereafter TSS, for ‘Third Signature Slope’, taking up the term ‘third signature’ proposed by ? to name the velocity shifts of spectral lines. An example of the linear fit corresponding to the TSS of HD223171 is shown in Fig. 3). In the following we focus on the analysis of the TSS computed over all spectra of a given star.

2.5. Sources of dispersion or biases

2.5.1. Telluric lines

Telluric lines caused by water may impact the line position estimation. Water wavelengths have been extracted from the HITRAN database ?, Jrothman13 available at <http://hitran.org/>. We listed the telluric lines which are within 0.02 Å of the lines used in our analysis. Most of these lines are very weak and are more than one order of magnitude lower than the stronger lines. Out of the 197 final lines used to compute the TSS in our selection, 5.5% have water telluric lines within 0.02 Å and the percentage decreases to 3% when only considering lines that are used in all six samples (i.e. lines that are most likely to highly impact the TSS estimations). The residual of RV versus F after subtracting the linear fit (used to determine the TSS) is not correlated with the position of telluric lines nor with their amplitude. We therefore estimate that the impact on our results should be negligible.

2.5.2. Wavelength dependence

Fig. 3 shows the RV versus depth for two different wavelength ranges for HD223171. There is a clear shift between the two sets of points; lines at shorter wavelengths tending to show larger blueshifts. We observe this effect on most of our stars as well as for the Sun. Note that the difference between the average RV of the black and red dots on the figure is of the order of 10 m/s only, while the shift in RV between the two straight lines is one order of magnitude larger. Such an effect has already been identified by ? and later by ?, using 298 FeI lines, and for the Sun in both cases. This effect is usually neglected in stellar studies ?, Jallendeprieto02 or not relevant because of the small wavelength coverage ?, Jgray09 but could explain some differences we observe with the differential velocity shift of ?, in particular the difference in shape which may be a wavelength effect and the much larger dispersion when considering more lines.

We measured this effect for a large sample of stars for the first time. To quantify this effect, we proceeded as follows: we considered a simple linear relationship between wavelength and RV and subtracted from the RV values a factor equal to $p_\lambda \times \lambda$, where p_λ is fitted to obtain a minimal rms of the RV residual after the wavelength- and depth- dependance correction. The rms being extremely sensitive to outliers, we performed this compu-

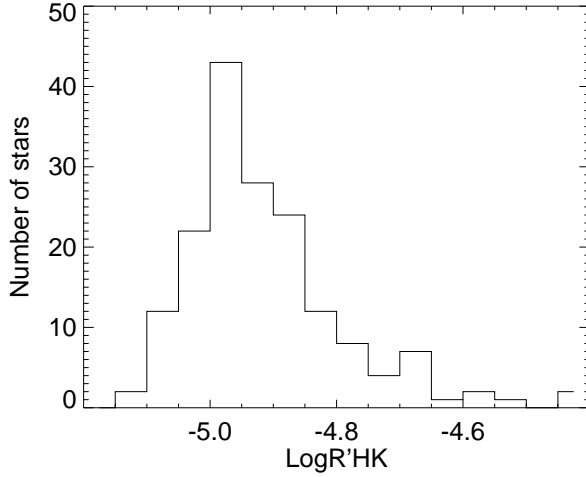


Fig. 4. Distribution of the LogR'_{HK} values in our sample (one average per star).

tation 100 times for half of the measurements only (which were picked up randomly in the original data set), which also allowed us to derive uncertainties. We then considered the average of the 100 values to estimate p_λ and derive the uncertainties from the distribution of the values. We find values of p_λ between -0.05 and 0.011 m/s/Å typically. The amplitude is compatible with the results of ? and ? for the Sun. We conduct a detailed analysis of this effect in Sect. 3.3.

2.5.3. Wavelength uncertainties

As pointed out by ?, laboratory wavelength uncertainties have a strong impact on RV determination. The FeII and TiI laboratory wavelengths we used in this work may lead to imprecisions of the order of 6 m/s at, for example, 5000 Å, which is small compared to the observed dispersion. However, most of the FeI wavelength uncertainties are probably one order of magnitude larger and may account for some of the observed dispersion ?, Jnave94,hamilton99. For the example shown in Fig. 3, the quadratic difference between the rms of the residuals for the two categories is 62 m/s.

2.6. Activity level

The activity level for each epoch computed using the classical LogR'_{HK} derived from the flux in the Ca II H and K lines, gives the Log of the chromospheric emission. Our values have been corrected using the HARPS-Mt Wilson correcting factor of ?. We did not introduce any correction for the thorium leaks, but we estimate that this should not impact our results significantly since we have selected spectra with a good signal to noise ratio and therefore with a large incoming flux. We have not taken into account the metallicity effect either. The distribution of the LogR'_{HK} values (averaged for each star) is shown in Fig. 4.

? studied 131 of the same stars included in our sample and there is a good correlation between the two estimates of LogR'_{HK} . Our computation leads to values approximately 0.5% smaller (i.e. a difference of the order of 0.025) than those derived by ?. This difference is not due to the difference in temporal coverage. Our LogR'_{HK} could be slightly biased due to the presence of thorium leaks or to the different spectrum selection, as well as

to different B-V values. Nevertheless, this does not impact our conclusion.

2.7. Analysis

The analysis performed in Sect. 3 allows us to study the dependence of the TSS on both the spectral type (or B-V / Teff) and on the activity level. The TSS and averaged LogR'_{HK} values for each star are shown in Table 1. For each spectral type, we compute the slope of the TSS versus LogR'_{HK} .

In a second part of the analysis (Sect. 4 and 5), we use the TSS to derive an average convective blueshift for each star. We consider the Sun as a reference, using the solar spectra obtained by ? and reduced in 2005 by Kurucz³. This allows us to derive RV temporal variations for each star following different assumptions, which may be compared to the actual RV variations.

3. Analysis of the differential velocity shifts of spectral lines

3.1. Dependence on B-V and Teff

The upper panel of Fig. 5 show the TSS versus B-V. The TSS characterises the slope of the differential velocity shifts of spectral lines and is strongly correlated with B-V (coefficient of 0.88, also meaning a strong anti-correlation with Teff). If we extrapolate the TSS towards larger B-V (smaller Teff), it reaches zero for B-V=1.04 (and Teff=4680 K). Fig. 5 also shows the TSS averaged over bins in B-V: there may be a trend for a saturation of the TSS at low B-V, but this would need to be confirmed with a study of more massive stars.

3.2. Dependence on activity

Fig. 6 shows the TSS versus LogR'_{HK} for all stars, colour-coded depending on their spectral types. We observe that for a given LogR'_{HK} , —TSS— is above a minimal value which decreases as the activity level increases. This minimum value is around 1000 m/s/(F/Fc) (in the following the TSS is in m/s/(F/Fc) where F/Fc represents the flux normalised to the continuum) for the less active stars, and then decreases towards a few hundred m/s/(F/Fc) for the most active stars in our sample.

After subtraction of the B-V dependency derived in the previous section (using a linear fit), the TSS residuals are shown on the lower panel of Fig. 5. These residuals are correlated with LogR'_{HK} (coefficient of 0.63), with a slope of 540 ± 30 m/s/(F/Fc). After correction of this LogR'_{HK} dependency, the rms on the TSS residuals is about 80 m/s/(F/Fc). It is still larger than the formal errors on the individual TSS values (estimated when performing the linear fit to compute the TSS and based on the RV and F uncertainties) by a factor of a few units, however, showing that other effects influence the TSS.

For LogR'_{HK} lower than ~ -4.85 , the slope of the residual TSS versus LogR'_{HK} is probably larger than the global slope, while for more active stars the trend may not be as significant: there could be in fact two regimes, one in which the TSS is very dependent on the activity level (for the less active stars, with a slope of 872 ± 39 m/s/(F/Fc)), and one in which the TSS is less dependent on activity (with a slope of 519 ± 78 m/s/(F/Fc)), suggesting different properties of the magnetic fields. Note that in this description the Sun would be at the edge of the non-active star domain with LogR'_{HK} values between -4.95 and -4.85.

³ <http://kurucz.harvard.edu/sun/fluxatlas2005/>

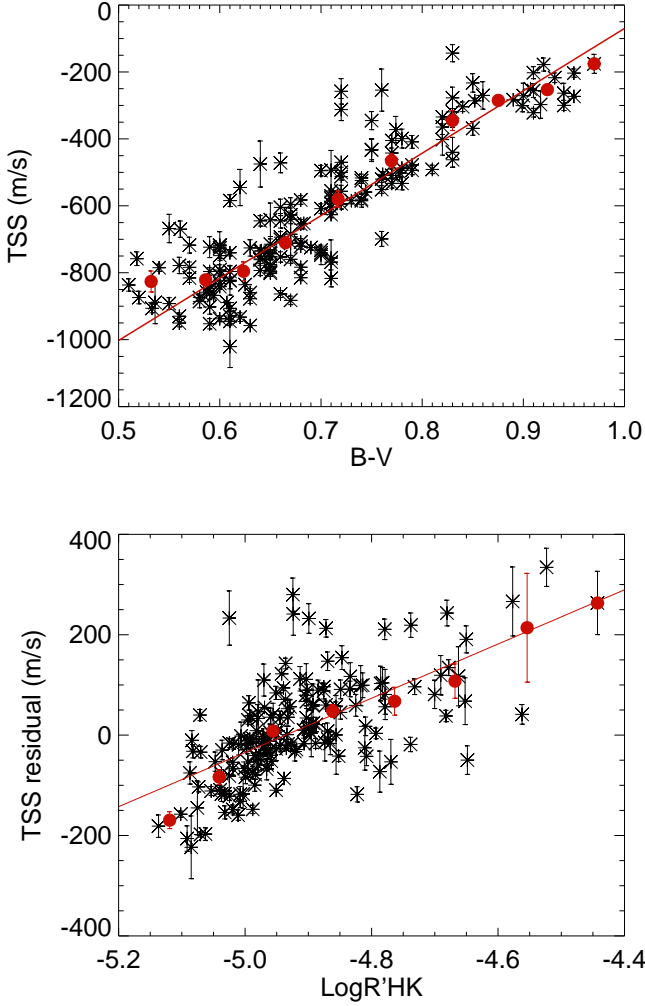


Fig. 5. *Upper panel:* TSS (slope of the differential velocity shifts of spectral lines, in m/s/(F/Fc)) versus the B-V of the stars. The solid line indicates a linear fit while the red dots correspond to TSS averaged over bins in B-V. *Lower panel:* Residual of the TSS after correction of the B-V dependence versus LogR'_{HK}. The solid line is a linear fit to the TSS.

We have noted in Sect. 2.6 that our LogR'_{HK} values were slightly smaller than those of \odot , by approximately 0.5%, with a large dispersion. This may impact the slope TSS (or TSS residuals) versus LogR'_{HK}. A difference of 0.5% impacts the slope with the same amplitude. If we recompute these slopes for each star sample, when there remains enough stars in common, we find larger slopes with differences between 0.5 and 20% (although the number of stars is smaller): our conclusions are therefore not significantly affected by this possible discrepancy.

3.3. Dependence on wavelength

Fig. 7 shows the p_λ factor defined in Sect. 2.5.3 versus the TSS and Teff for our star sample. p_λ characterises the amplitude of the dependency of differential velocity shifts on the wavelength. We find a strong correlation between this factor and the amplitude of the TSS and with Teff, at least for Teff larger than 5400 K. The dispersion is, however, quite large for low Teff, which may be due to the very small signal in that domain. p_λ is equal to

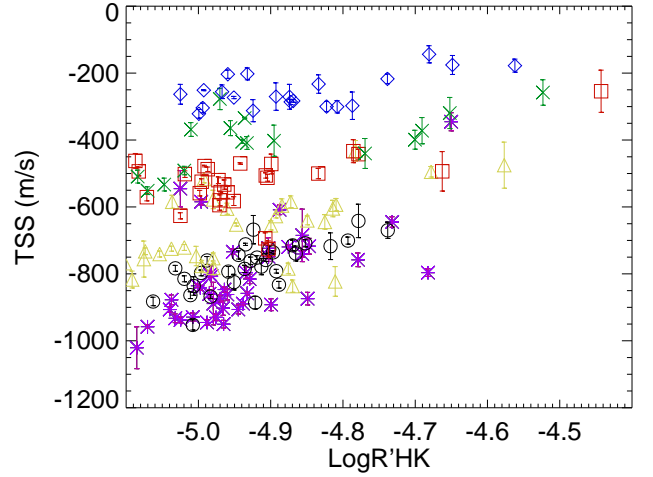


Fig. 6. TSS (slope of the differential velocity shifts of spectral lines, in m/s/(F/Fc)) versus LogR'_{HK} for all stars in each sample (same colour and symbol codes as in Fig. 2).

0.124 m/s/Å for the solar spectrum: this solar value is compatible with the results in Fig. 7 since it is very close to the values obtained for stars at the same Teff. The impact of this effect on the TSS is significant: for example it decreases from -863 m/s/(F/Fc) to -1163 m/s/(F/Fc) for HD223171 and from -799 m/s/(F/Fc) to -1107 m/s/(F/Fc) for the Sun.

Finally, we subtract the Teff dependence from p_λ and show the residuals versus LogR'_{HK} in Fig. 7 (lower panel). The rms of the residuals is 0.017 m/s/Å. We find that the activity level impacts the maximum value which can be taken by the slope so that high activity levels reduce the wavelength dependence, at least for G stars.

Both the Teff and the LogR'_{HK} impacts on p_λ represent strong constraints for the simulation of stellar convection over a large grid of stars, with or without magnetic fields. The wavelength dependence is likely to be due to the stronger contrast of granulation towards lower wavelengths, reinforcing the convective blueshift. This interpretation agrees with our observed trends as a function of Teff and activity, and such measurements may provide constraints on granulation contrasts.

3.4. Analysis for each spectral type

The average TSS was computed for each of the six star samples. The results are shown in Table 2, and on Fig. 8 (upper panel). There is a clear decrease of the TSS towards cooler stars, as seen above. The TSS corrected for the wavelength dependence is also shown and appears larger in amplitude but shows a similar trend.

We now consider the dependence of the TSS on the activity level separately for each spectral type in our sample. The TSS versus the average LogR'_{HK} is shown in Fig. 9, with a positive correlation in all cases. There are however some deviations from the linear fit. This could be due to the fact that the temperatures of the stars vary within a given sample, as well as to inclination effects (see Sect. 4.3 for a discussion). The possible uncertainty in spectral classification could also lead to some dispersion or outliers if some stars are in fact subgiants of luminosity class IV, or have been incorrectly classified. Stellar rotation may also impact our estimates \odot , as discussed for example by Ramirez09: after taking into account the fact that both the TSS and the rota-

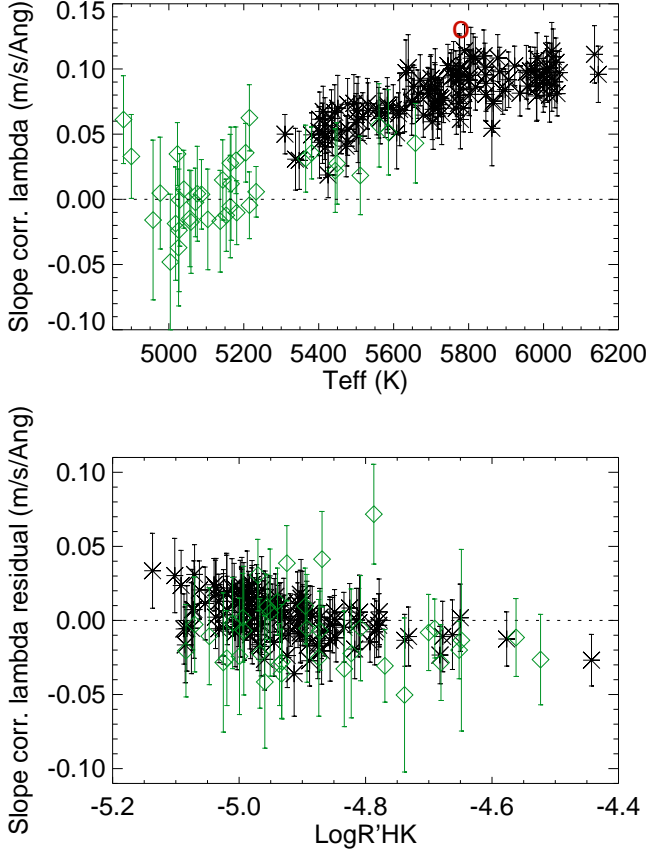


Fig. 7. *Upper panel:* Slope of the wavelength dependence factor p_λ of the differential velocity shifts versus T_{eff} for G (black stars) and K (green diamonds) stars. The solar value of p_λ is 0.124 and is shown as a red circle. *Lower panel:* Same for the p_λ residuals after correction of the T_{eff} relationship versus LogR'_{HK} .

Table 2. Main results: TSS and activity and wavelength dependencies

Sample	TSS	σ TSS	Slope	σ Slope	p_λ
	(m/s /(F/Fc))	(m/s /(F/Fc))	(m/s /(F/Fc))	(m/s /(F/Fc))	(m/s/Å (m/s/Å))
G0	-811.7	20.8	829.5	44.0	0.092
G2	-774.1	12.9	672.3	57.7	0.086
G5	-672.3	19.7	466.8	56.6	0.077
G8	-523.2	17.2	349.0	62.3	0.056
K0	-402.1	22.6	318.4	49.8	0.026
K2	-254.3	11.2	231.0	40.0	-0.006

Notes. For each spectral type there is shown: the TSS (without the wavelength correction), the slope of TSS versus LogR'_{HK} associated to its uncertainties and the wavelength factor p_λ . The TSS is the slope of the differential velocity shifts of spectral lines.

tion rates vary with spectral type, we find that the TSS residuals do not show any significant trend versus $v_{\text{sin}i}$ for our sample limited to $v_{\text{sin}i}$ lower than 5 km/s. We do not, therefore, expect a strong bias in this $v_{\text{sin}i}$ range. On the other hand, we also expect the differential rotation to impact the TSS, as shown by ? for ex-

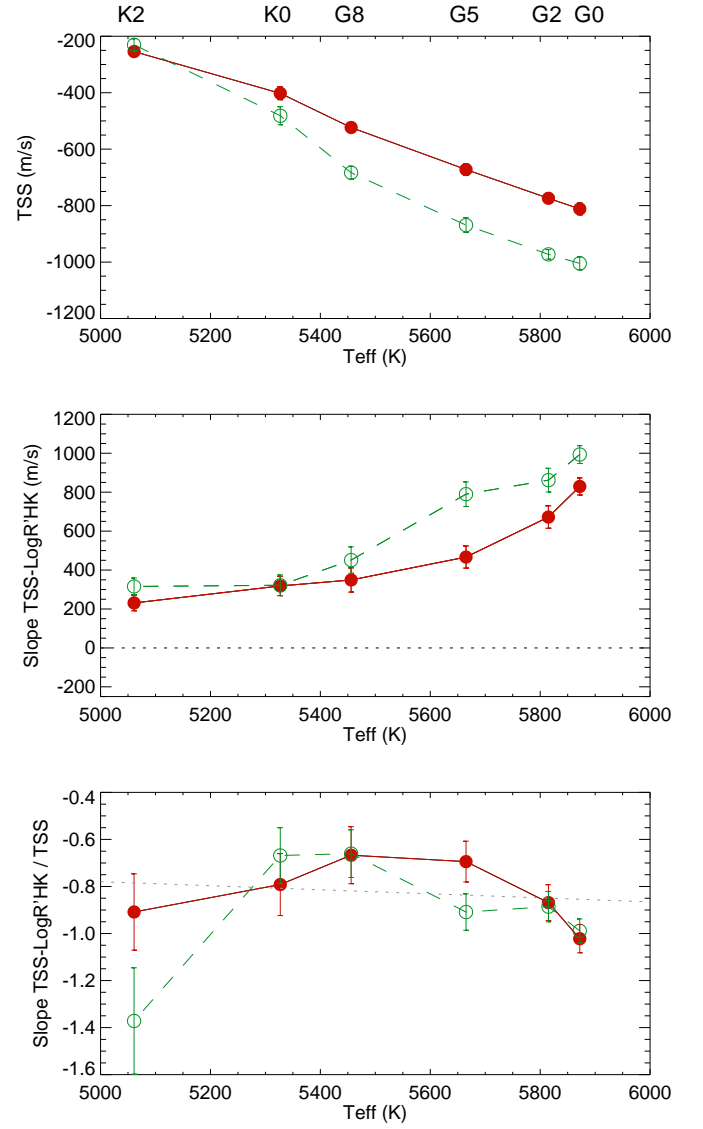


Fig. 8. *Upper panel:* TSS (slope of the differential velocity shifts of spectral lines, in m/s/(F/Fc)) averaged for each sample versus the average temperature of the sample (red filled circles and solid line). The green curve (open circles and dashed line) shows the TSS after the wavelength dependence correction. *Middle panel:* Same for the slope of the TSS versus LogR'_{HK} . *Lower panel:* Same for the ratio between this slope and the TSS. The dotted line is a linear fit on the ratio in red.

ample, and believe that this effect, though difficult to quantify, could add some dispersion.

The slope of the TSS versus the average LogR'_{HK} is shown in Fig. 8 (values are indicated in Table 2) and is smaller for cooler stars while it can be as large as 800 m/s/(F/Fc) for G0 stars. This corresponds to an amplitude of 80 m/s/(F/Fc) for an amplitude of 0.1 of the LogR'_{HK} (i.e. a typical difference in LogR'_{HK} between solar cycle minimum and maximum). An extrapolation of the slope with T_{eff} gives a zero TSS for $T_{\text{eff}}=4830$ K, which is close to the values derived for the TSS.

Finally, the ratio between this slope and the TSS (i.e. between the curves from panels 1 and 2 of Fig. 8) is shown on the lower panel: this ratio, showing the attenuation factor of the convective blueshift due to activity, does not show any strong trend, suggesting that stars of different types probably have a very sim-

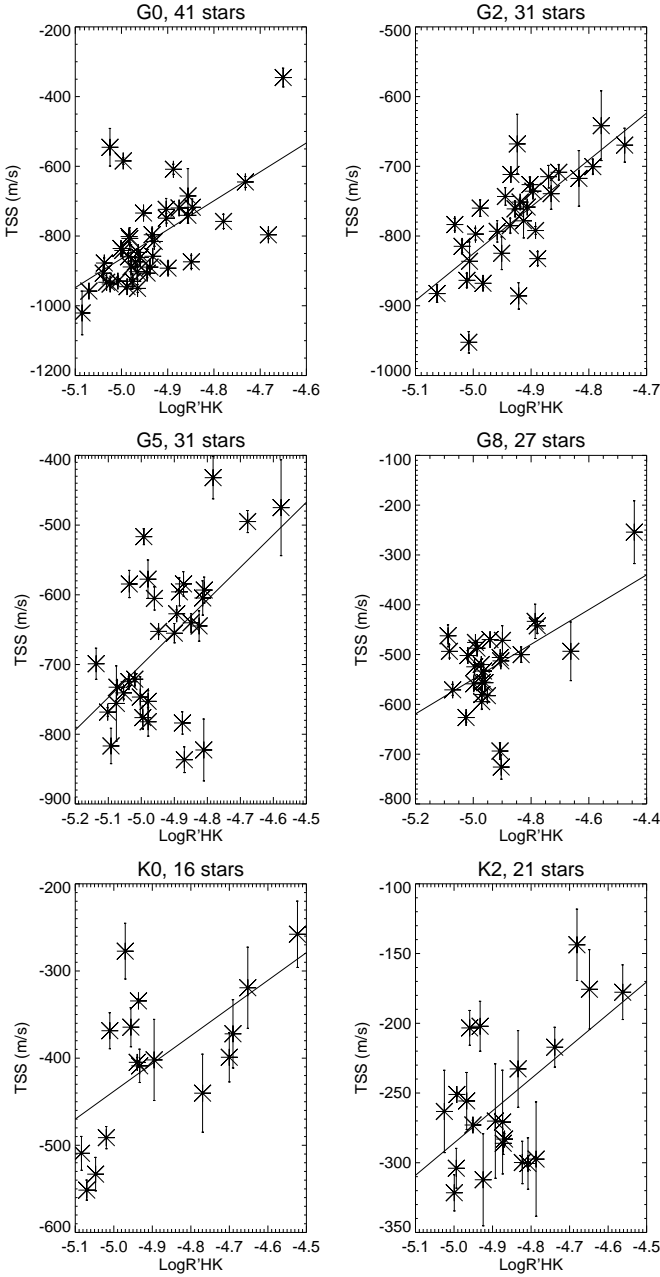


Fig. 9. Each panel shows the TSS (slope of the differential velocity shifts of spectral lines, in $\text{m/s}/(F/F_c)$) computed for each star versus the average LogR'_{HK} of that star. The straight line is a linear fit on the measurements.

ilar response to magnetic activity relative to the amplitude of convection, that is, the convection may be reduced within the same proportions.

We can compare this last result with the simulations made by ?. Their hydrodynamic simulation of granulation in the presence of small scale magnetic fields for stars from F3 to M2 shows a magnetic field strength independant from the spectral type, so that if more flux is available, it is spread over a larger surface. Such a behaviour has also been observed by ? on a small range of simulation parameters. In such conditions we would expect the response in terms of granulation properties (and hence the convective blueshift) to be similar from one spectral type to another, since the magnetic field properties do not change much, which is what we observe.

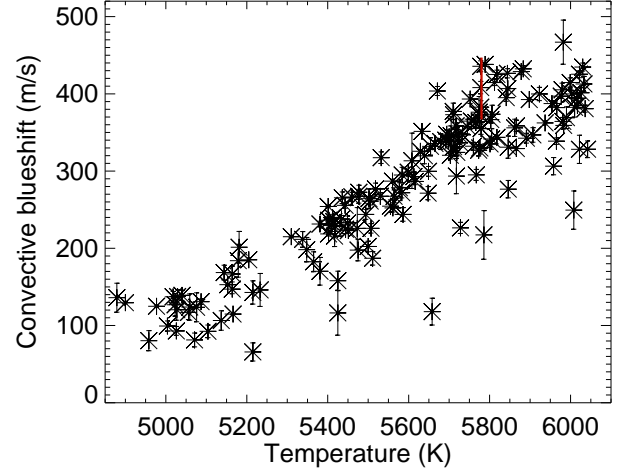


Fig. 10. Reconstructed convective blueshift versus T_{eff} for all stars in our sample. The vertical red line corresponds to the solar convective blueshift derived from Reiners et al. (2016) for no weighting and for a weighting equal to the line depth.

4. Convective blueshifts

In Sect. 1 we mentioned two related effects of convection on spectral line shifts: the absolute convective shift, which is relevant for the exoplanet RV analysis for example (RV typically computed over all available spectral lines), but difficult to measure directly, and the differential shifts measured in the previous section. To derive the former from differential shift measurements such as the TSS, we need to make some assumptions and use the Sun as a reference.

4.1. Computed convective blueshifts

In this section, we use the TSS computed for each star to estimate its convective blueshift, using two principles:

- We use the assumption made by ? that the shape of the differential shift of spectral lines is representative of the absolute convective blueshift due to granulation that we are interested in. In this same publication this factor is computed between the curve for a given star and the solar curve used as a reference, and is also used to derive the intrinsic radial velocity of these stars: their results show a proportionality between the shape, or in our case the slope, and the absolute convective blueshift. In principle it would be possible to check such an assumption with output from numerical simulations such as those provided by ? for K stars or by ? for a larger range of stellar parameters, since they compute shifts from a large set of spectral lines leading to both differential and absolute values. Unfortunately, however, they do not attempt to check that assumption.
- We use the Sun as a reference. For that purpose, we need two solar values: the solar TSS_⊙ and the convective blueshift $RV_{\text{convbl}\odot}$. We derive the solar TSS_⊙ from the solar spectrum of ? using the set of lines we used for the G2 sample. However, the spectral resolution of this spectrum is 500,000, that is, approximately four times larger than the resolution of HARPS spectra (approx. 120,000): ? pointed out that a degraded resolution has a significant impact on slopes such as the TSS we derive for resolution below 200,000, leading

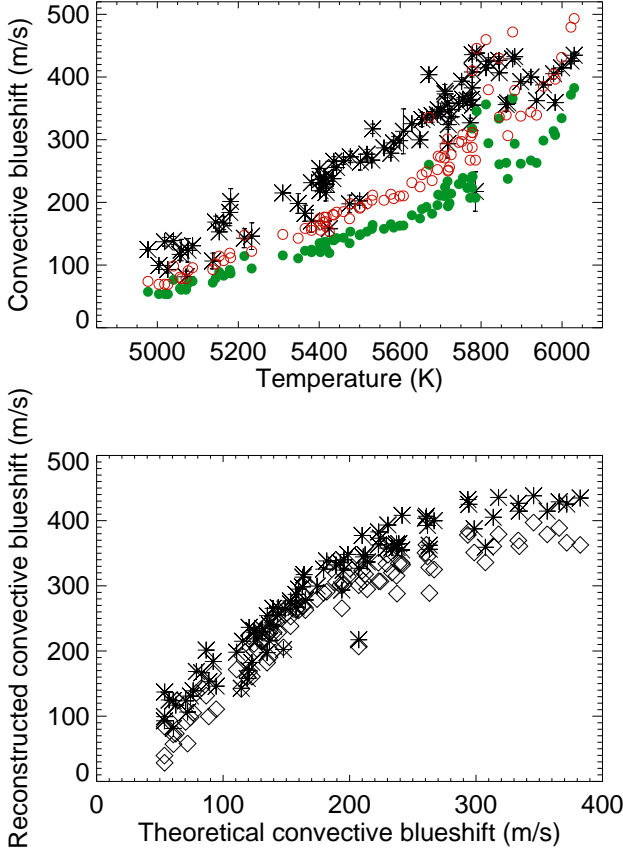


Fig. 11. *Upper panel:* Reconstructed convective blueshift versus Teff for the stars for which the formula of Allende Prieto et al. (2013) could be applied (stars). The convective blueshift derived from Allende Prieto et al. (2013) for those stars is shown before correction from the wavelength range (red circle) and after correction (green dots). *Lower panel:* Reconstructed convective blueshift versus those derived from Allende Prieto et al. (2013), from the original TSS (stars) and those corrected for the wavelength dependence (diamonds).

to smaller slopes (approx. 25% for the HARPS resolution). We have therefore also computed $TSS_{\odot} = -776 \text{ m/s}/(F/F_{\odot})$, the difference with the original value being smaller than what was derived by Hamilton 99. We use the value of $-776 \text{ m/s}/(F/F_{\odot})$ in the following. As for the solar convective blueshift, a value of 300 m/s, Dravins 99 is often used, for example in Meunier 10. It corresponds to the values measured over all lines taken into account in classical RV computations such as those commonly performed. This estimation is however uncertain, for example due to uncertainties in laboratory wavelengths. We have recently reevaluated an absolute RV versus spectral line depth for the Sun (i.e. similar to what we have done in Sect. 3 but for absolute- rather than relative RV). Unfortunately, they do not provide the average convective blueshift that corresponds to their results. Using their relationship between the absolute RV and line depth, and a sample of spectral lines we extract from the solar spectrum of ? for depths between 0.05 and 0.95 and wavelengths between 4000 and 6600 Å, we obtain an average convective blueshift of 435 m/s (i.e. larger than the previous value of

300 m/s). If we assume that when computing the RV using cross-correlations between spectra, the RV is more sensitive to deep lines (we assume a weighting factor equal to the line depth), we obtain a convective blueshift of 355 m/s. In the following we consider this the value to compute the convective blueshift. It should be multiplied by 1.22 if we wish to consider a convective blueshift based on average-between-spectral-line positions rather than a weighted one.

The convective blueshift of each star is therefore computed as follows:

$$RV_{\text{convbl}} = TSS \times RV_{\text{convbl}\odot} / TSS_{\odot}, \quad (1)$$

where TSS is the stellar value derived in Sect. 3 and the solar values are as discussed above. Fig. 10 shows the resulting convective blueshifts for all stars in our sample versus Teff. There is naturally a strong correlation since our convective blueshift is proportional to the TSS. There may also be a plateau for Teff larger than 5800 K. Note that the convective blueshifts derived from the TSS corrected for the wavelength effect (not represented on the figure) are only 38 m/s lower than the original ones, so the effect is small.

4.2. Comparison of the adopted convective blueshift with theoretical results

We now wish to compare our computed values with theoretical results.

? performed hydrodynamical simulations of granulation for various star parameters to deduce a number of properties for the exploitation of GAIA observations, including a numerical expression of the convective blueshift of stars depending on their Teff, log g and metallicity. The formula only being valid for certain ranges in parameters, we have only been able to apply their formula to 93 stars in our sample. The red dots in Fig. 11 represent the theoretical convective blueshift for these stars based on the stellar parameters of ?, while our estimation is represented by the black stars. This convective blueshift corresponds to the GAIA wavelength range, that is, 8470-8740 Å. If we compute the solar convective blueshift from the results of ? as above but selecting only lines in this wavelength range, we obtain 459 m/s (computation with line depth weighting) instead of the 355 m/s obtained above. Therefore, to be representative of a large wavelength range RV computation, this theoretical convective blueshift should be divided by 1.29, as shown by the green dots. On the other hand, applying the formula of ? to the solar parameters leads to a convective blueshift of 285 m/s, which is significantly smaller than 459 m/s deduced from the observation of ? for the same wavelength range suggesting that the numerical simulations produce a convection significantly weaker (by a factor of approximately 1.7 below 5800 K) than that observed.

When comparing the simulated convective blueshift (green dots) with the estimated convective blueshift based on the assumption of Sect. 4.1, we naturally find a significant difference in amplitude as well, since the Sun was used as a reference. That said, the trend for Teff lower than 5800 K is similar, except for the multiplying factor (a factor of approximately 2). Above 5800 K, the trend seems different, with a strong increase observed in the simulation but not in our observations: this will need to be investigated in the future.

? also provide line shifts versus Teff from numerical simulations of stellar convection as well, with a similar trend in Teff. Their line shifts are approximately 100 m/s at 5000 K (similar to our values) but in the range 700-800 m/s at 6000 K, that is,

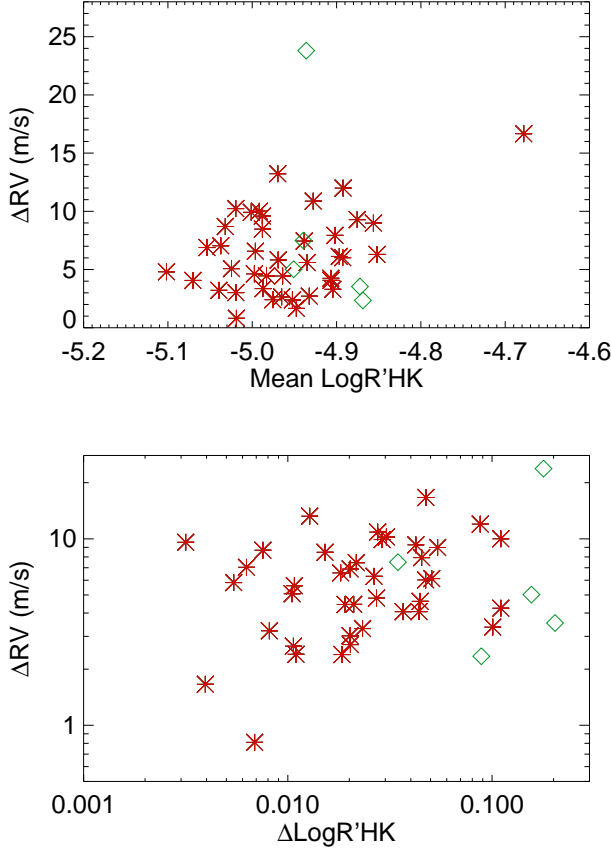


Fig. 12. *Upper panel:* ΔRV_{obs} versus the average LogR'_{HK} , computed on the binned time series and for the 43 stars with more than two bins (see text), for G (red stars) and K (green diamonds) stars. *Lower panel:* Same versus $\Delta \text{LogR}'_{\text{HK}}$

slightly larger than our values and much larger than those of ?. This could be due to the fact that their line shifts are computed from the bottom of the line (and not for the whole line, as is assumed in the convective blueshift definition here), and/or may correspond to the specific fictitious Fe I line they are using meaning that a direct comparison of the amplitudes is difficult. An interesting feature observed by ? however is a saturation appearing at temperatures larger than 6000 K, which may be similar to what we observe.

5. RV variability

We now wish to compare the observed RV variability (derived in Sect. 5.1) with those which can be predicted using our estimated TSS (in Sect. 5.2). We have thus retrieved the radial velocities computed by the ESO Data Reduction Software from the headers of the archive files. These RV must be corrected for two effects:

- 36 stars in our sample bear planets according to the Extrasolar Planets Encyclopaedia⁴. We therefore retrieved the exoplanet parameters, fitted the parameters when not published (this is sometimes the case for the time at periastron and periastron argument), reconstructed the corresponding RV time series, and finally subtracted the plane-

tary signal from the measured RV . Note that some of these stars bear several planets (22 with 1 planet, 9 with 2 planets, 3 with 3 planets and 1 with 4 planets). One of them has not been corrected because the three planets are all below 1 m/s. This is a necessary step, otherwise the induced RV is overestimated and in some cases possible correlation with the LogR'_{HK} may be masked by the presence of the planetary signal. In most cases the parameters have been retrieved from the compilation made by ?. Others were taken from elsewhere ?, Jbutler06,naef07,pepe11,hinkel15,diaz16, and parameters not provided have been fitted on our time series.

- A very strong RV trend with time is exhibited by six particular stars suggesting the presence of a binary. We have removed the trend before analysing their RV (using a linear fit or a second degree polynomial fit).

5.1. Observed RV versus LogR'_{HK}

When only considering stars with at least 10 observations (131 stars), 40% of the stars have a correlation between RV and LogR'_{HK} above 0.4 and 24% above 0.6. To compute long-term amplitudes, we averaged the RV values in 50 day bins. We made sure to have at least 5 points in each bin (otherwise the observation was discarded) and considered stars with at least 4 such bins in the following analyses. This reduced our sample to 43 stars. From these time series we computed the RV amplitude (defined as the maximum minus the minimum of the binned time series), ΔRV_{obs} , as well as $\Delta \text{LogR}'_{\text{HK}}$ and the average LogR'_{HK} for comparison purposes. ΔRV_{obs} is compared in the next section with RV variations derived from the convective blueshift. Considering stars with more bins considerably reduces the sample, although the statistics, in terms of stars with a good correlation between RV and LogR'_{HK} , are relatively robust: 40% of the stars have a correlation between RV and LogR'_{HK} (from the binned series). The uncertainties on each RV measurement as computed by the ESO Data reduction Software are between 0.2 and 0.6 m/s depending on the star. Because there is also some stellar intrinsic variability and since some bins contain as few as five points, the uncertainties on ΔRV are larger, typically of the order of 1-2 m/s.

Fig. 12 shows ΔRV_{obs} versus the averaged LogR'_{HK} for each of the 43 stars (which shows no particular trend) and versus the amplitude of the LogR'_{HK} . We see that strong variations in RV tend to be associated with stronger amplitudes in LogR'_{HK} , although there is a large dispersion.

Our results can be compared with previous RV variations published in the literature. Most of the time only the rms of RV (before binning) versus the average of the LogR'_{HK} or R'_{HK} (and not the amplitude, which we believe is more relevant) is available. Our rms RV falls well within the range of variation of ? and ?, although we also observe stars with smaller rms. Furthermore, we find, as they do, that there is no clear trend when considering the rms versus the average R'_{HK} . This is different from the results of ? and ?, who found larger rms and a trend. We have also computed the slope of R'_{HK} versus RV (before binning) as studied by ? as a function of T_{eff} . Our slopes are of similar amplitudes in the different T_{eff} domains.

The Sun, with an amplitude of logR'_{HK} of 0.1 and a predicted amplitude in RV of 8 m/s ?, jmeunier10a falls within the range of values found for our sample.

⁴ <http://exoplanet.eu/>

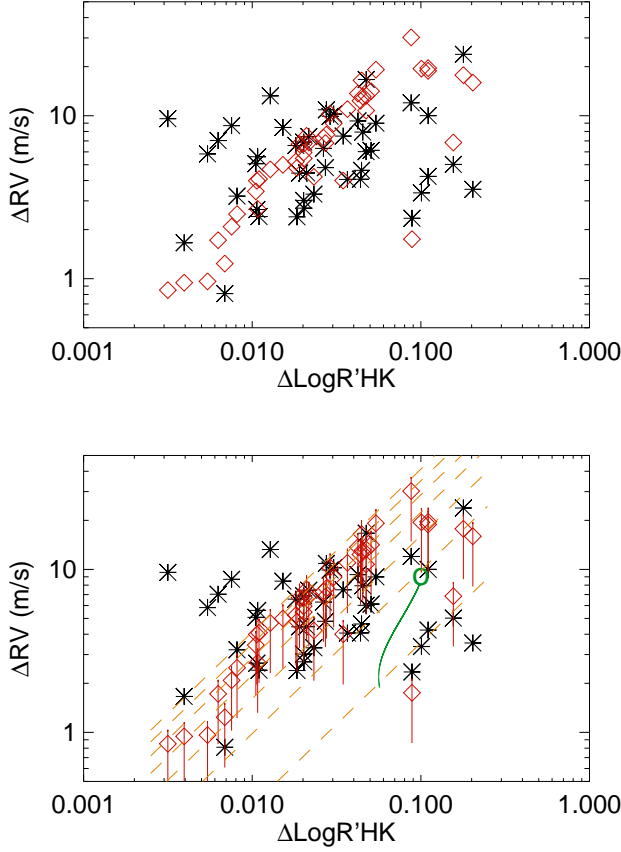


Fig. 13. *Upper panel:* ΔRV_{obs} versus the amplitude of the LogR'_{HK} , on averaged time series (see text), in black. ΔRV_{conv} is shown in red. *Lower panel:* Same as the upper panel. Red vertical lines correspond to the ΔRV_{conv} reconstructed for inclinations of the rotational axis in the range 10–90°. The green circle is the solar value (seen equator-on), and the green line indicates what the solar value would be for various inclinations. The orange dashed line corresponds to ΔRV_{conv} reconstructed from eq. 5 for T_{eff} between 4950 K (lower curve) and 6150 K (higher curve) with a step of 200 K between each curve.

5.2. Simulated RV

5.2.1. Computation of the simulated RV

We now estimate the RV variations that would be due to the attenuation of the convective blueshift from the typical dependence of the convective blueshift on activity and from the amplitude of variation of the logR'_{HK} for each star. For a given spectral type, we defined in Sect. 3.4 the slope of the TSS versus LogR'_{HK} , hereafter referred to as G . Hence, if a certain star activity level varies with $\Delta \text{LogR}'_{\text{HK}}$, then we expect a variation of ΔTSS_o of the TSS, the ratio being the slope :

$$G = \Delta \text{TSS}_o / \Delta \text{LogR}'_{\text{HK}_o}. \quad (2)$$

For this star, following eq. 1, the convective blueshift is:

$$RV_{\text{convbl}_o} = \text{TSS}_o \times RV_{\text{convbl}_o} / \text{TSS}_o. \quad (3)$$

As a consequence, for any star we study with the same temperature (i.e. corresponding to the same G) and with an observed variability of $\Delta \text{LogR}'_{\text{HK}_*}$, we expect the TSS to vary by:

$$\Delta \text{TSS}_* = G \times \Delta \text{LogR}'_{\text{HK}_*}. \quad (4)$$

In the following, R will be interpolated for each T_{eff} from the curve in Fig. 8. From eqs. 1 and 4, the variation of the convective blueshift with time (i.e. the RV variation due to the attenuation of the convective blueshift) is:

$$\Delta RV_{\text{conv}} = G \times RV_{\text{convbl}_o} / \text{TSS}_o \Delta \text{LogR}'_{\text{HK}}. \quad (5)$$

ΔRV_{conv} is then compared with ΔRV_{obs} (derived in Sect. 5.1) and plotted as a function of $\Delta \text{LogR}'_{\text{HK}}$ in Fig. 13 (upper panel). The global amplitude corresponds to observations. We note that ΔRV_{conv} is not correlated with ΔRV_{obs} however, although the amplitudes are compatible, meaning that for a given star the reconstructed value can be quite different from the observed one. This could be due to the fact that eq. 5 does not include any dependence on inclination of the stellar rotational axis and therefore we assume in the following that it corresponds to an inclination of 45°, as the slope G for a given spectral type has been computed for a sample of stars with various random inclinations.

5.2.2. Impact of inclination on the estimation

The way we estimated the impact of inclination is detailed in Appendix C. The results are shown in Fig. 13 (bottom panel) as red lines. When taking into account the impact of inclination on our reconstructed ΔRV_{conv} , the obtained dispersion and range of values correspond well to the observations. Note that the ranges have been computed assuming solar activity patterns: for a star with a different latitude distribution of magnetic activity (i.e. close to the equator, or on the contrary able to extend more poleward) we expect the laws such as those shown in Fig. C.2 to be slightly different, leading to slightly different ranges. We conclude that a large part of the observed dispersion can be explained by the various inclinations of the stars in our sample.

For comparison purposes, Fig. 13 also shows the curves corresponding to eq. 5 for seven values of T_{eff} spanning our sample (orange dashed line), starting with 4950 K (bottom line) and then with increasing T_{eff} (with a step of 200 K) up to 6150 K. The green circle indicates the position of the Sun, and its track for various inclinations as computed by ?. The Sun is localised at a relatively low position compared to other stars of similar temperature and to the straight line corresponding to 5750 K. However, the stars in our sample which fall within the same T_{eff} range all exhibit $\Delta \text{LogR}'_{\text{HK}}$ lower than 0.05, therefore it is not straightforward to extrapolate their behaviour for a larger variability such as the one observed for the Sun. We conclude that inclination allows for a large dispersion in RV amplitude for a given activity variability.

6. Conclusion

We have defined a criterion to characterise the differential velocity shift of spectral lines for a sample of 167 main sequence stars with spectral types in the range K2 to G0. We estimate the slope of RV versus the flux F at the bottom of each spectral line ?, studied byfor the Sun]dravins81, which we named the TSS, versus the spectral type, the activity level and wavelength. We focus on temporally averaged properties. Our conclusions are as follows:

- We find a decreasing TSS and therefore a decreasing convective blueshift amplitude with decreasing temperature, as expected, with a convective blueshift of approximately 150 m/s for K2 stars and 500 m/s for G0 stars. The derived convective

blueshift based on the assumption made by ? that the convective blueshift is proportionnal to the shape (the slope in our case) of the differential velocity shifts shows a trend with temperature which is in close agreement with the granulation simulations of ? but twice larger in amplitude for temperatures lower than 5800 K. There is also a discrepancy in the trend for the highest temperature (above 5800K), suggesting further analysis is needed, as there may be a saturation effect not visible in the simulation by ? but obtained by ?.

- We find, for the first time, a significant and strong variation of the TSS (and hence of the convective blueshift) with the average activity level of the star in the K2 to G0 domain.
- The relative variations of the TSS with activity, that is, the slope of the TSS variation with LogR'_{HK} divided by the average TSS for that spectral type, are relatively constant with spectral type. Therefore the TSS variations with activity are proportional to the amplitude of the convective blueshift for all spectral types. A constant attenuation factor is compatible with the MHD simulations performed by ?.
- We derive an amplitude of RV variations due to the convective blueshift (including a possible range corresponding to different inclination assumptions) from the estimated convective blueshift and observed LogR'_{HK} variations. This amplitude is compared with the observed RV variations for the stars of our sample. We find a global agreement in term of amplitude. The effects of temperature and inclination ?, following the inclination study for the Sun of Jorgensen 15 aptly explain the observed dispersion, except in the domain of small activity variability, in which some of our RV amplitudes may be overestimated.
- ? and ? showed that, for the Sun, the RV depends on wavelength, clearly visible when taking into account the F dependence. We generalise these results and observe this dependence for the first time for a large sample of main sequence stars. The amplitude of the effect decreases towards smaller temperatures, and disappears for our K2 sample. It also decreases as activity increases.

The results obtained in this paper will allow us to perform realistic simulations of RV temporal series for various types of stars, following the work of ? for the Sun.

Acknowledgements. This work has been funded by the Université de Grenoble Alpes project called "Alpes Grenoble Innovation Recherche (AGIR)" and by the ANR GIPSE ANR-14-CE33-0018. This work made use of several public archives and databases: The HARPS data have been retrieved from the ESO archive at http://archive.eso.org/wdb/wdb/adp/phase3_spectral/form. This research has made use of the SIMBAD database, operated at CDS, Strasbourg, France. The telluric line properties were retrieved from the HINTRAN database. Exoplanets information was retrieved from the Extrasolar Planet Encyclopaedia at <http://exoplanet.eu/>. The solar spectrum from Kurucz et al. (1984) is available on-line at <http://kurucz.harvard.edu/sun/fluxatlas2005/>.

Appendix A: Additional tables

Appendix B: Continuum correction: procedure

The procedure is as follows:

- We define an upper envelope for each spectrum by retrieving the highest intensity in each 5 \AA bin. We eliminate outliers that may be due to cosmics by performing a linear fit on eleven such adjacent points and removing the point with the largest residual. For each remaining point, we recompute the linear fit and consider the residual after the fit removal at that point. The distribution of these values is fitted with a gaussian. Points with values outside a $3\text{-}\sigma$ range or too close to each other are also eliminated. The resulting intensities versus wavelength are then smoothed and interpolated on the original list of wavelengths, providing an upper envelope for the spectrum.
- The spectrum is then divided by this upper envelope. The distribution of all intensities in the spectrum peaks at the level of the continuum (its position depends on the noise level). This provides a correcting factor, by which the spectra is multiplied to provide the final spectra, normalised to a continuum of 1. A visual examination shows that the continuum can be slightly off in a few wavelength ranges. The effect is larger for low S/N spectra.

Note that in principle the correcting factor depends on the wavelength, as the S/N depends on the order. However the impact on our analysis is very limited, especially since we have considered lines in the $5000\text{-}6855 \text{ \AA}$ range only.

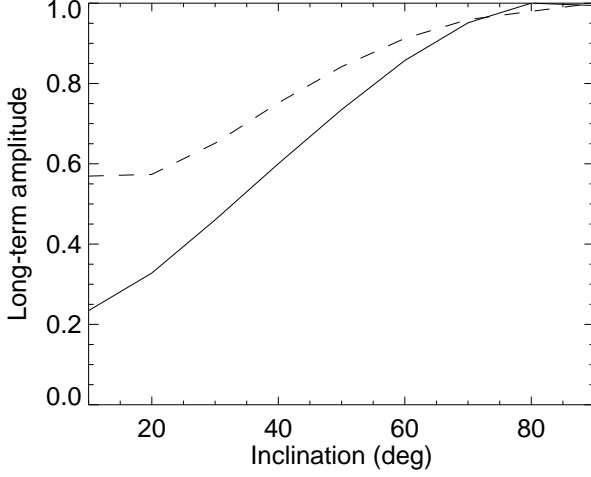


Fig. C.1. Dependence of the attenuation of the long-term convective blueshift ΔRV_{conv} versus inclination f_{RV} (solid line), normalised to one, for a solar simulation (from Borgniet et al. 2015), and variation of the corresponding plate coverage f_{fit} (dashed line), also normalised.

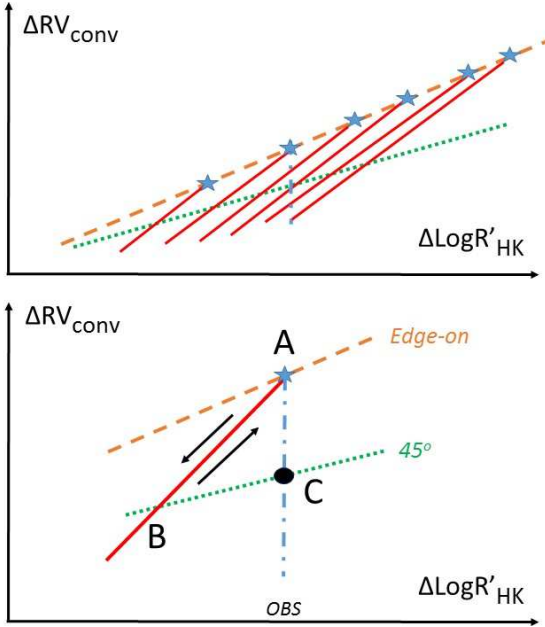


Fig. C.2. *Upper panel:* Schematic view of ΔRV_{conv} versus $\Delta \text{Log} R'_{\text{HKObs}}$ showing the impact of inclination for a star at a given temperature and different activity levels: seen equator-on (orange dashed line with blue stars), at 45° (dotted green line). The red tracks correspond to the various inclinations for each blue star. The vertical dotted-dashed blue thick line corresponds to the various ΔRV_{conv} that would correspond to different inclinations for a given observed $\Delta \text{Log} R'_{\text{HKObs}}$. *Lower panel:* Same zoomed in on one particular observation (see text).

Appendix C: Impact of inclination on the RV variability

We now consider the dependence of the rotational axis on inclination. ? have studied the impact of inclination on the RV time series from a solar simulation for various inclinations. The RV and plate coverage (which is directly related to the chromospheric emission) are maximal for a Sun seen equator-on and minimal for a pole-on configuration. They do not vary by the same factor however: a factor of 4.2 for RV and a factor of 1.8 for the plate coverage. In the following we will apply this RV factor f_{RV} to our computed RV to derive a reconstructed RV at a given inclination to another. We apply the plate coverage factor f_{fit} to $\text{Log} R'_{\text{HK}}$ as well. Normalised f_{RV} and f_{fit} are shown on Fig. C.1.

We now estimate the impact of this dependence on our reconstructed ΔRV_{conv} . Let us first consider a star, with a given T_{eff} , seen equator-on (as the Sun). Depending on the amplitude of activity variability of this star, it will be located at different positions in the $(\Delta \text{Log} R'_{\text{HK}}, \Delta RV_{\text{conv}})$ diagram, and will follow the orange line in Fig. C.2 (upper panel), different blue stars corresponding to specific $\Delta \text{Log} R'_{\text{HK}}$. If the same stars were seen with an inclination of 45° , they would be located on the black line, whose slope

is defined by G (defined in Sect. 5.2.1, for the T_{eff} of the star). One of these stars with a given activity level but seen at different inclinations would follow one of the red tracks. When we reconstruct ΔRV_{conv} as above, we do not know the inclination of the star, only the amplitude of variation of the $\text{Log} R'_{\text{HK}}$. Given an observed $\Delta \text{Log} R'_{\text{HKobs}}$, the reconstructed ΔRV_{conv} for various inclinations should therefore be at any location along the vertical thick blue line (close to the top if seen edge on, and close to the bottom if seen pole-on), that is, where the vertical line crosses any red track.

We therefore wish to compute the values corresponding to this blue segment for each of our stars, to estimate the value it would take for all possible inclinations. Note that our computations are made for inclinations between 10 and 90°; the range covered by the simulation of ?. On Fig. C.2 (lower panel), the black dot at C is the reconstructed ΔRV_{conv} from eq. 5 applied to the observed $\Delta \text{Log} R'_{\text{HKobs}}$. As an example, let us consider how to reconstruct ΔRV_{conv} for an equator-on configuration, that is, for point A, which has the same observed $\Delta \text{Log} R'_{\text{HKobs}}$. This star is then on the red track: if it was seen at a different inclination (i.e. from another observer's point of view) it would be along this track. Such an observer observing it at 45° would therefore see point B, which has the following coordinates:

$$\Delta \text{Log} R'_{\text{HK}}(B) = \Delta \text{Log} R'_{\text{HKobs}} \times f_{\text{ff}}(45^\circ) / f_{\text{ff}}(90^\circ). \quad (\text{C.1})$$

$\Delta RV_{\text{conv}}(B)$ is derived from eq. 5 applied to $\Delta \text{Log} R'_{\text{HK}}(B)$. From this point B, we can move along the track back to point A by applying the RV correcting factor to the point B RV amplitude:

$$\Delta RV_{\text{conv}}(A) = \Delta RV_{\text{conv}}(B) \times f_{\text{RV}}(90^\circ) / f_{\text{RV}}(45^\circ) \quad (\text{C.2})$$

The same computation, using eqs. C.1 and C.2 but applied to any inclination instead of 90° will provide the range of ΔRV_{conv} covering all inclinations between 10 and 90°.

Table 1. Star properties

Name	Sp. t.	B-V	Teff (K)	N _{Spectra}	TSS (m/s/(F/Fc))	σ TSS (m/s/(F/Fc))	LogR' _{HK}	σ LogR' _{HK}	Conv. Blueshift (m/s)
HD1388	G0	0.59	5954	123	-846.9	7.9	-4.964	0.001	500.
HD3823	G0	0.56	6022	64	-929.9	9.8	-4.976	0.001	549.
HD4307	G0	0.61	5812	68	-906.5	8.7	-5.040	0.001	535.
HD11505	G0	0.63	5752	22	-859.6	12.2	-4.985	0.001	507.
HD14374	G0	0.75	5425	8	-345.3	26.9	-4.650	0.014	204.
HD20807	G0	0.60	5866	176	-719.5	5.5	-4.876	0.001	425.
HD21938	G0	0.55	5778	20	-892.1	17.7	-4.899	0.001	526.
HD27063	G0	0.64	5767	30	-645.0	15.6	-4.732	0.004	381.
HD31527	G0	0.59	5898	231	-858.1	4.7	-4.932	0.000	506.
HD31822	G0	0.57	6042	44	-717.5	23.7	-4.847	0.001	423.
HD32724	G0	0.61	5818	30	-929.2	12.2	-5.008	0.002	548.
HD36379	G0	0.56	6030	71	-950.3	11.4	-4.965	0.001	561.
HD38973	G0	0.59	6016	33	-861.5	16.8	-4.960	0.002	508.
HD39091	G0	0.58	6003	83	-874.1	10.4	-4.970	0.001	516.
HD44447	G0	0.53	5999	30	-906.3	13.3	-4.945	0.001	535.
HD52265	G0	0.54	6136	6	-888.7	63.5	-4.979	0.007	524.
HD67458	G0	0.60	5891	25	-748.8	14.0	-4.903	0.003	442.
HD68978A	G0	0.61	5965	123	-740.5	9.2	-4.856	0.002	437.
HD71479	G0	0.63	6026	31	-877.4	14.5	-5.037	0.003	518.
HD73524	G0	0.60	6017	138	-841.5	7.3	-4.997	0.001	496.
HD78558	G0	0.57	5711	31	-815.5	13.6	-4.929	0.001	481.
HD88218	G0	0.60	5878	67	-937.5	8.8	-5.025	0.001	553.
HD88742	G0	0.59	5981	31	-796.4	11.3	-4.682	0.009	470.
HD96700	G0	0.61	5845	309	-889.2	3.8	-4.938	0.000	525.
HD97037	G0	0.61	5883	87	-945.2	8.3	-4.988	0.001	558.
HD105837	G0	0.52	5907	23	-758.0	20.5	-4.779	0.003	447.
HD114729	G0	0.62	5844	47	-932.6	13.1	-5.032	0.001	550.
HD117618	G0	0.60	5990	10	-807.0	30.7	-4.982	0.002	476.
HD134060	G0	0.62	5966	280	-835.6	5.2	-5.001	0.001	493.
HD143114	G0	0.61	5775	20	-796.3	16.8	-4.934	0.001	470.
HD147512	G0	0.73	5530	29	-584.5	9.5	-4.996	0.005	345.
HD150433	G0	0.64	5665	67	-733.9	8.1	-4.952	0.001	433.
HD183658	G0	0.65	5803	43	-801.5	9.2	-4.984	0.002	473.
HD197210	G0	0.70	5577	16	-608.4	14.4	-4.888	0.007	359.
HD198075	G0	0.59	5846	10	-723.4	31.4	-4.903	0.005	427.
HD204385	G0	0.59	6033	20	-902.3	21.4	-4.966	0.003	532.
HD206172	G0	0.67	5608	2	-684.9	78.4	-4.856	0.007	404.
HD213240	G0	0.61	5982	3	-1020.7	62.5	-5.085	0.005	602.
HD210752	G0	0.52	5923	20	-874.0	18.8	-4.849	0.001	516.
HD215456	G0	0.63	5789	181	-957.8	5.1	-5.070	0.001	565.
HD216435	G0	0.62	6008	12	-545.3	54.1	-5.025	0.004	322.
HD1320	G2	0.65	5679	13	-739.2	22.4	-4.865	0.004	436.
HD2071	G2	0.68	5719	49	-708.5	10.9	-4.852	0.003	418.
HD20619	G2	0.66	5703	34	-700.5	10.6	-4.793	0.005	413.
HD28701	G2	0.61	5710	14	-824.7	23.4	-4.951	0.002	487.
HD37962	G2	0.65	5718	3	-641.7	50.0	-4.779	0.014	379.
HD38858	G2	0.64	5733	201	-758.5	4.3	-4.907	0.001	448.
HD45289	G2	0.68	5717	71	-783.4	8.7	-5.032	0.001	462.
HD59711A	G2	0.64	5722	47	-761.0	11.4	-4.928	0.002	449.
HD71334	G2	0.67	5694	42	-759.9	11.8	-4.988	0.001	448.
HD78429	G2	0.60	5760	58	-726.2	10.9	-4.902	0.004	428.
HD88084	G2	0.64	5766	22	-793.2	15.4	-4.959	0.001	468.
HD93385	G2	0.59	5977	214	-867.8	6.3	-4.983	0.001	512.
HD95521	G2	0.65	5773	22	-714.8	16.2	-4.870	0.008	422.
HD102365	G2	0.67	5629	257	-711.7	3.3	-4.935	0.000	420.
HD104982	G2	0.65	5692	36	-743.2	12.5	-4.944	0.001	439.
HD108309	G2	0.68	5775	48	-814.7	8.9	-5.019	0.002	481.
HD121504	G2	0.60	6022	8	-717.3	39.9	-4.817	0.012	423.
HD125881	G2	0.60	6036	66	-832.4	9.9	-4.889	0.002	491.
HD145666	G2	0.56	5958	17	-669.7	24.3	-4.738	0.003	395.
HD145809	G2	0.59	5778	30	-952.4	15.4	-5.008	0.001	562.
HD146233	G2	0.65	5818	329	-751.3	5.8	-4.919	0.001	443.
HD168871	G2	0.54	5983	116	-785.1	10.6	-4.936	0.000	463.
HD177758	G2	0.56	5862	18	-778.2	24.5	-4.913	0.002	459.
HD189567	G2	0.64	5726	203	-735.7	4.6	-4.897	0.001	434.
HD193193	G2	0.58	5979	24	-885.9	18.9	-4.921	0.003	523.

HD196800	G2	0.59	6010	19	-836.2	27.7	-5.006	0.002	493.
HD207129	G2	0.60	5937	257	-792.0	5.6	-4.892	0.002	467.
HD208487	G2	0.55	6146	19	-667.8	42.4	-4.924	0.003	394.
HD210918	G2	0.65	5755	63	-797.2	8.5	-4.996	0.002	470.
HD213575	G2	0.67	5671	24	-882.5	12.7	-5.063	0.002	521.
HD223171	G2	0.66	5841	62	-863.5	10.2	-5.011	0.002	510.
HD967	G5	0.61	5564	21	-584.4	17.5	-4.872	0.002	345.
HD8828	G5	0.74	5403	35	-516.7	11.3	-4.992	0.001	305.
HD8859	G5	0.71	5502	7	-577.5	27.5	-4.980	0.002	341.
HD12387	G5	0.66	5700	20	-752.9	15.4	-4.979	0.003	444.
HD16141	G5	0.71	5806	5	-816.8	25.4	-5.092	0.007	482.
HD16714	G5	0.71	5518	15	-605.2	16.6	-4.960	0.003	357.
HD19034	G5	0.67	5477	14	-595.8	20.0	-4.884	0.004	352.
HD20407	G5	0.57	5866	27	-783.8	15.9	-4.876	0.001	462.
HD28471	G5	0.65	5745	14	-782.1	20.6	-4.979	0.005	461.
HD50806	G5	0.71	5633	73	-768.2	6.2	-5.102	0.001	453.
HD66428	G5	0.71	5705	2	-755.8	53.9	-5.075	0.022	446.
HD78538	G5	0.64	5786	3	-475.0	68.8	-4.577	0.036	280.
HD78747	G5	0.51	5778	39	-836.6	18.4	-4.870	0.001	494.
HD89454	G5	0.70	5728	40	-494.9	15.8	-4.678	0.004	292.
HD90156	G5	0.68	5599	124	-652.5	4.6	-4.948	0.000	385.
HD96423	G5	0.69	5711	63	-724.6	7.5	-5.037	0.001	428.
HD104263	G5	0.74	5477	20	-584.5	19.5	-5.036	0.003	345.
HD107148	G5	0.70	5805	4	-746.7	29.1	-5.003	0.002	441.
HD110619	G5	0.67	5613	24	-640.2	13.3	-4.849	0.008	378.
HD111031	G5	0.70	5801	38	-732.6	9.9	-5.074	0.001	432.
HD115674	G5	0.68	5649	23	-655.1	13.8	-4.900	0.004	387.
HD124364	G5	0.66	5584	13	-644.7	21.8	-4.825	0.010	380.
HD161098	G5	0.67	5560	100	-627.2	5.6	-4.893	0.002	370.
HD189625	G5	0.66	5846	17	-604.6	24.6	-4.814	0.011	357.
HD190647	G5	0.76	5639	11	-698.9	22.3	-5.137	0.002	412.
HD204313	G5	0.68	5776	67	-721.0	8.8	-5.020	0.002	425.
HD220507	G5	0.70	5698	79	-740.7	8.9	-5.054	0.001	437.
HD222422	G5	0.75	5475	6	-432.0	30.4	-4.783	0.008	255.
HD222582	G5	0.65	5779	25	-776.1	16.3	-4.996	0.004	458.
HD222595	G5	0.71	5648	20	-593.2	18.6	-4.809	0.013	350.
HD224393	G5	0.61	5774	4	-822.5	44.4	-4.811	0.020	485.
HD10700	G8	0.72	5310	438	-469.9	2.3	-4.942	0.000	277.
HD20003	G8	0.77	5494	36	-533.1	13.8	-4.964	0.008	315.
HD20794	G8	0.71	5401	491	-555.6	2.4	-4.969	0.000	328.
HD21411	G8	0.71	5473	2	-493.5	58.9	-4.663	0.007	291.
HD37986	G8	0.79	5507	28	-493.7	13.3	-5.083	0.002	291.
HD45364	G8	0.76	5434	53	-520.0	10.1	-4.972	0.002	307.
HD69830	G8	0.79	5402	596	-477.9	2.4	-4.992	0.001	282.
HD85119	G8	0.76	5425	2	-254.2	63.0	-4.443	0.010	150.
HD94151	G8	0.72	5583	22	-594.6	14.9	-4.971	0.007	351.
HD97343	G8	0.78	5410	51	-501.9	9.8	-5.019	0.001	296.
HD98281	G8	0.76	5381	65	-505.9	7.9	-4.907	0.005	298.
HD111232	G8	0.68	5460	30	-582.5	13.1	-4.951	0.001	344.
HD123265	G8	0.83	5338	7	-462.4	22.2	-5.087	0.006	273.
HD124292	G8	0.74	5443	41	-558.8	8.4	-4.998	0.001	330.
HD132648	G8	0.72	5418	17	-500.2	15.5	-4.834	0.011	295.
HD136894	G8	0.74	5412	37	-524.5	8.7	-4.995	0.001	309.
HD145598	G8	0.66	5417	7	-471.6	29.5	-4.899	0.001	278.
HD157172	G8	0.78	5451	89	-487.2	6.6	-4.987	0.004	287.
HD161612	G8	0.71	5616	41	-626.5	9.2	-5.025	0.001	370.
HD167359	G8	0.75	5348	3	-433.3	34.5	-4.786	0.021	256.
HD172513	G8	0.77	5500	33	-442.3	15.0	-4.779	0.004	261.
HD196761	G8	0.72	5415	44	-512.8	10.2	-4.904	0.003	303.
HD210277	G8	0.71	5505	23	-570.8	11.1	-5.071	0.003	337.
HD213628	G8	0.72	5555	18	-556.4	17.8	-4.960	0.003	328.
HD213941	G8	0.66	5532	30	-693.7	16.4	-4.907	0.006	409.
HD214385	G8	0.63	5654	15	-725.8	24.4	-4.903	0.003	428.
HD224619	G8	0.74	5436	16	-580.2	16.5	-4.970	0.003	342.
HD870	K0	0.77	5381	2	-372.1	39.2	-4.691	0.008	220.
HD9796	K0	0.82	5179	4	-402.1	46.6	-4.895	0.019	237.
HD26965	K0	0.82	5153	395	-334.4	2.3	-4.936	0.002	197.
HD39194	K0	0.77	5205	141	-404.8	5.6	-4.939	0.001	239.
HD72579	K0	0.77	5449	16	-509.2	19.4	-5.084	0.002	300.
HD74014	K0	0.76	5561	22	-551.4	11.5	-5.070	0.001	325.

HD80883	K0	0.83	5233	3	-319.3	46.6	-4.652	0.020	188.
HD83443	K0	0.79	5511	15	-408.8	19.2	-4.933	0.014	241.
HD90711	K0	0.81	5444	23	-491.2	12.7	-5.019	0.008	290.
HD90812	K0	0.82	5164	5	-364.5	22.4	-4.956	0.007	215.
HD104006	K0	0.83	5023	6	-277.2	32.0	-4.970	0.003	164.
HD130322	K0	0.78	5365	3	-399.0	28.2	-4.700	0.001	235.
HD176157	K0	0.83	5181	2	-440.2	44.8	-4.769	0.008	260.
HD202605	K0	0.72	5658	2	-257.9	38.0	-4.523	0.001	152.
HD203384	K0	0.78	5586	13	-533.1	19.2	-5.047	0.006	315.
HD220256	K0	0.85	5144	8	-368.6	20.6	-5.010	0.003	217.
HD17970	K2	0.84	5040	14	-304.0	14.3	-4.994	0.006	179.
HD40307	K2	0.95	4977	337	-272.9	3.4	-4.951	0.003	161.
HD82516	K2	0.91	5104	24	-202.1	17.9	-4.932	0.010	119.
HD101930	K2	0.91	5164	21	-321.6	13.0	-4.999	0.010	190.
HD106275	K2	0.90	5059	6	-270.8	37.2	-4.874	0.035	160.
HD129642	K2	0.95	5026	31	-203.3	12.5	-4.959	0.003	120.
HD130930	K2	0.94	5027	4	-263.2	29.5	-5.025	0.013	155.
HD154577	K2	0.89	4900	294	-283.1	3.9	-4.869	0.002	167.
HD176986	K2	0.94	5018	29	-299.8	15.2	-4.823	0.005	177.
HD192031	K2	0.72	5215	2	-312.2	33.0	-4.924	0.005	184.
HD192310	K2	0.91	5166	1230	-251.0	1.6	-4.993	0.001	148.
HD209742	K2	0.85	5137	7	-232.7	27.5	-4.834	0.021	137.
HD204941	K2	0.91	5056	16	-255.7	20.4	-4.967	0.007	151.
HD44573	K2	0.92	5071	14	-177.7	19.6	-4.562	0.005	105.
HD68607	K2	0.83	5215	7	-143.7	25.6	-4.681	0.013	85.
HD23356	K2	0.93	5004	10	-217.2	14.3	-4.738	0.004	128.
HD148303	K2	0.97	4958	8	-175.6	28.4	-4.648	0.022	104.
HD220339	K2	0.90	5029	11	-300.6	18.5	-4.808	0.017	177.
HD13808	K2	0.85	5087	66	-286.1	8.0	-4.872	0.010	169.
HD65562	K2	0.86	5076	3	-270.1	41.0	-4.893	0.022	159.
HD203850	K2	0.92	4879	2	-297.4	41.0	-4.787	0.008	175.

Notes. Star name, spectral type and B-V from the CDS, Teff from ?, number of spectra used in the analysis, TSS and its 1- σ uncertainty, averaged LogR'_{HK} and its 1- σ uncertainty and the convective blueshift derived from the TSS in Sect. 4.1 (without the wavelength correction).

Table 1. Sample lines

Wavelength (Å)	Element	Nb. sample
4999.5000	TiI	2
5001.8636	FeI	6
5002.7927	FeI	6
5005.7123	FeI	6
5014.9425	FeI	5
5016.1600	TiI	6
5016.4790	FeI	4
5022.2355	FeI	6
5022.8700	TiI	6
5024.8400	TiI	6
5027.7567	FeI	6
5028.1264	FeI	6
5030.7786	FeI	2
5036.4600	TiI	6
5038.4000	TiI	6
5039.9600	TiI	6
5040.6100	TiI	2
5043.5800	TiI	3
5044.2114	FeI	6
5045.4100	TiI	2
5048.4361	FeI	6
5049.8198	FeI	4
5062.1000	TiI	2
5064.6500	TiI	6
5067.1496	FeI	6
5068.7658	FeI	6
5072.0784	FeI	6
5072.6721	FeI	6
5074.7483	FeI	6
5078.9748	FeI	6
5079.2230	FeI	6
5079.7400	FeI	6
5083.3386	FeI	6
5085.3300	TiI	1
5090.7740	FeI	6
5107.4474	FeI	5
5109.6520	FeI	6
5125.8345	FeI	1
5127.3593	FeI	6
5131.4687	FeI	6
5133.6885	FeI	4
5137.3822	FeI	6
5141.7390	FeI	6
5151.9109	FeI	6
5152.1800	TiI	6
5159.0576	FeI	6
5162.2729	FeI	6
5165.4107	FeI	5
5173.7400	TiI	5
5187.9142	FeI	6
5191.4550	FeI	4
5192.9700	TiI	6
5194.0300	TiI	1
5194.9418	FeI	6
5195.4723	FeI	6
5196.0596	FeI	6
5198.7111	FeI	6
5215.1806	FeI	6
5216.2740	FeI	6
5217.3893	FeI	6
5223.6200	TiI	1
5224.5400	TiI	4
5225.5261	FeI	6
5226.8623	FeI	3
5228.3767	FeI	6
5234.6200	FeII	6

5242.4911	FeI	6
5246.5500	TiI	1
5247.0504	FeI	6
5250.2089	FeI	6
5250.6460	FeI	6
5253.4617	FeI	6
5263.3063	FeI	6
5264.8000	FeII	5
5266.5554	FeI	1
5273.1636	FeI	6
5273.3736	FeI	6
5364.8713	FeI	6
5365.3991	FeI	6
5367.4668	FeI	6
5373.7086	FeI	6
5383.3692	FeI	3
5389.4792	FeI	6
5393.1676	FeI	4
5404.1516	FeI	1
5410.9098	FeI	6
5415.1993	FeI	4
5426.2500	TiI	1
5434.5238	FeI	4
5445.0424	FeI	6
5446.5829	TiI	4
5446.9168	FeI	1
5453.6400	TiI	1
5460.5000	TiI	2
5462.9595	FeI	6
5466.3962	FeI	6
5473.9005	FeI	6
5474.2200	TiI	1
5476.5642	FeI	6
5481.8600	TiI	1
5487.7460	FeI	6
5501.4653	FeI	6
5503.9000	TiI	1
5506.7791	FeI	6
5511.7800	TiI	1
5525.5443	FeI	6
5534.8400	FeII	5
5560.2116	FeI	6
5562.7065	FeI	6
5565.7040	FeI	6
5569.6181	FeI	4
5576.0888	FeI	6
5624.5422	FeI	4
5633.9465	FeI	6
5638.2621	FeI	6
5648.5600	TiI	1
5655.4900	FeI	6
5662.9380	TiI	6
5679.0229	FeI	6
5686.5302	FeI	6
5701.5446	FeI	6
5715.0986	TiI	6
5739.4700	TiI	1
5752.0320	FeI	6
5775.0806	FeI	6
5785.9800	TiI	1
5804.2600	TiI	1
5862.3565	FeI	6
5880.2700	TiI	1
5903.3100	TiI	1
5905.6720	FeI	6
5916.2474	FeI	6
5918.5300	TiI	3
5922.1100	TiI	3
5927.7891	FeI	4
5930.1799	FeI	6

5937.8100	TiI	1
5941.7500	TiI	3
5952.7184	FeI	6
5956.6944	FeI	6
5976.7771	FeI	6
5983.6810	FeI	6
6008.5566	FeI	6
6027.0509	FeI	6
6056.0047	FeI	6
6064.6200	TiI	1
6065.4822	FeI	6
6078.4911	FeI	6
6091.1700	TiI	1
6102.1777	FeI	6
6127.9066	FeI	6
6136.6153	FeI	5
6136.9947	FeI	6
6157.7284	FeI	6
6173.3356	FeI	6
6191.5584	FeI	6
6213.4303	FeI	6
6219.2810	FeI	6
6226.7363	FeI	1
6229.2283	FeI	4
6230.7230	FeI	4
6232.6412	FeI	6
6240.6462	FeI	6
6246.3188	FeI	6
6247.5600	FeII	2
6252.5554	FeI	6
6256.3615	FeI	6
6258.1000	TiI	6
6265.1340	FeI	6
6270.2250	FeI	6
6290.9656	FeI	6
6293.9257	FeI	2
6302.4936	FeI	6
6303.7500	TiI	1
6312.2300	TiI	1
6318.0175	TiI	6
6322.6855	FeI	6
6335.3308	FeI	6
6380.7433	FeI	6
6392.5388	FeI	1
6393.6013	FeI	4
6408.0184	FeI	6
6419.9496	FeI	6
6421.3508	FeI	6
6430.8464	FeI	6
6494.9805	FeI	2
6546.2395	TiI	6
6569.2155	FeI	1
6581.2101	FeI	1
6592.9100	TiI	4
6592.9138	TiI	6
6599.1000	TiI	1
6625.0220	FeI	1
6633.7497	FeI	6
6663.4421	FeI	6
6743.1200	TiI	2

Notes. TiI and FeII wavelengths from ? and FeI wavelengths from ?, elements and number of spectral type samples in which the line has been used in our analysis.